On the Spectral Quality of Time-Resolved CMOS SPAD-Based Raman Spectroscopy With High Fluorescence Backgrounds

Jere Kekkonen, Tuomo Talala, Jan Nissinen, and Ilkka Nissinen, *Member, IEEE*

***Abstract*—The fluorescence background in Raman spectroscopy can be effectively suppressed by using pulsed lasers and time-gated detectors. A recent solution to reduce the high complexity and bulkiness of the time-gated systems is to implement the detector by utilizing time-resolved single-photon avalanche diodes (SPADs) fabricated in complementary-metal-oxide-semiconductor (CMOS) technology. In this study, we investigate the effects of fluorescence-to-Raman ratio, recording time and excitation intensity on the quality of Raman spectra measured by using one of the furthest developed fluorescence-suppressed Raman spectrometers based on a time-resolved CMOS SPAD line sensor. The objectives were to provide information on the significance of the different causes behind the distortion of the measured Raman spectra with various measurement conditions and to provide general information on the possibilities to exploit the high-intensity non-stationary pulsed laser excitation to gain additional improvement on the spectral quality due to laser-induced fluorescence saturation. It was shown that the distortion of the spectra with samples having short fluorescence lifetimes (~2 ns) and high fluorescence-to-Raman ratios, i.e. with challenging samples, is dominated by the timing skew of the sensor instead of the shot noise caused by the detected events. In addition, the actual reason for the observed improvement in the spectral quality as a function of excitation intensity was discovered not to be the conventionally thought increased number of detected photons but rather the laser-induced fluorescence saturation. At best, 26% improvement to the signal-to-noise ratio was observed due to fluorescence saturation.**

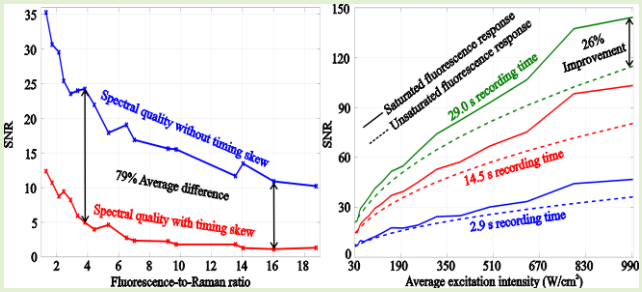

***Index Terms*—Raman spectroscopy, non-stationary laser-induced fluorescence saturation, complementary metal–oxide–semiconductor single-photon avalanche diode (CMOS SPAD), timing inhomogeneities, timing skew, spectral quality, signal-to-noise ratio (SNR), signal-to-distortion ratio (SDR).**

I. Introduction

RAMAN spectroscopy is a very powerful optical tool that can be used to nondestructively and quantitatively resolve the chemical and molecular composition of a sample. The potential of Raman spectroscopy has been recognized in various fields such as agricultural, food, forensic, security, biomedical and pharmaceutical sciences, just to name a few [1]–[5]. The main advantages of Raman spectroscopy are that it needs minimal sample preparation and it can be used to measure samples in all the states of matter [3], [4]. Furthermore, the interference of water in Raman spectra is relatively weak making Raman spectroscopy also a suitable tool for analyses of aqueous solutions [4].

The main challenge of Raman spectroscopy is the high fluorescence emission of some samples [6]. The fluorescence emission does not provide as detailed information on the molecular composition of a sample as Raman scattering does and thus, the fluorescence emission may be considered as competing phenomenon for Raman scattering in Raman spectroscopy. The intensity of fluorescence background is in many cases markedly higher than the intensity of Raman scattering masking partly or even totally the desired Raman spectra. Therefore, the fluorescence background often dramatically decreases the signal-to-noise ratio (SNR) of the recorded Raman spectra and the reduction of fluorescence background should be considered to play a crucial role in the further development of Raman spectroscopy techniques [7].

One very promising method to suppress the effect of fluorescence background is based on the time response difference

Manuscript received December 2, 2019; revised January 9, 2020; accepted January 9, 2020. Date of publication January 13, 2020; date of current version April 3, 2020. This work was supported by the Academy of Finland under Contract 314404, Contract 323719 and Contract 307362 (Centre of Excellence in Laser Scanning Research). The associate editor coordinating the review of this article and approving it for publication was Dr. Cheng-Ta Chiang. *(Corresponding author: Jere Kekkonen.)*

The authors are with the Circuits and Systems Research Unit, University of Oulu, 90014 Oulu, Finland (e-mail: jere.kekkonen@oulu.fi; tuomo.talala@oulu.fi; jan.nissinen@oulu.fi; ilkka.nissinen@oulu.fi).

Digital Object Identifier 10.1109/JSEN.2020.2966119

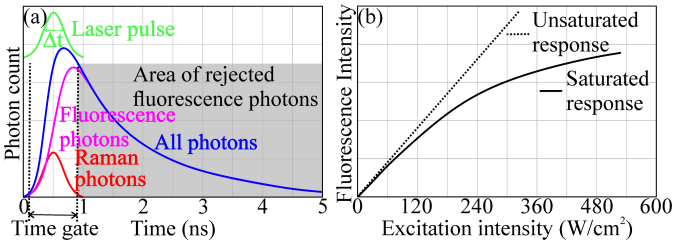

Fig. 1. (a) Time distributions of a laser pulse, Raman scattered photons and fluorescence emitted photons and the basic principle of fluorescence suppression by means of a time gating technique. (b) Saturated (solid line) and unsaturated (dotted line) fluorescence response as a function of excitation intensity.

between Raman scattering and fluorescence emission. Fluorescence emission decays with a typical lifetime close to 10 ns, whereas the Raman scattering is an instantaneous phenomenon [6], [8]. This time response difference can be utilized by illuminating the sample with a pulsed laser instead of conventional continuous wave (CW) laser and by collecting the photons only during the echo pulse from the sample (backscattering configuration) by means of a time-gated detector. Consequently, all the Raman photons generated by the laser pulse can be collected while most of the total fluorescence emission from the sample can be rejected as depicted in Fig. 1(a). Time-gated detectors have been implemented by means of techniques like ultra-fast intensified gated charge-coupled devices (CCD) and Kerr gates with detectors, for example, but the main drawbacks of time gating techniques have been their high complexity, bulkiness and costs that have hampered their widespread usage [9], [10].

A more recent and less complex technique to implement a time-gated detector is to use time-resolved single-photon avalanche diodes (SPADs) fabricated with a complementary-metal-oxide-semiconductor (CMOS) process as the detector of a compact fluorescence-suppressed Raman spectrometer [11],[12]. The time-resolved CMOS SPAD-based Raman spectroscopy follows the general principles of time-correlated single-photon counting (TCSPC) [13]. The main advantage of CMOS SPAD sensors is their high integration capability that enables to integrate all the necessary TCSPC electronics into a single integrated circuit with a SPAD-array reducing the size and complexity of the whole device [14]–[17]. The time-resolved CMOS SPAD sensors also make it possible to more practically realize the other functionalities for Raman spectroscopy, such as Raman radar and Raman depth profiling operations, which could open novel application possibilities in various fields [18], [19].

Unfortunately, all the fluorescence photons cannot be rejected even with the time gating techniques, and thus it is important to have a quantity to evaluate the performance of different Raman spectrometer setups. Normally, this quantity in Raman spectroscopy is the SNR, which is described by the ratio between detected Raman photons and shot noise caused by the total events, as shown below in (1):

$$SNR = \frac{N_R}{\sqrt{N_R + N_F + N_B}} \tag{1}$$

where N_R, N_F and N_B are the detected photon counts of Raman scattered, fluorescence emitted and background photons (including the dark counts of the detector) [12]. As mentioned, the effectiveness of the time gating techniques to improve the SNR is based on the reduction of the fluorescence photon count since this decreases the denominator (i.e. the shot noise) of (1) and consequently increases the SNR value. Another possibility to improve the SNR is to increase the overall photon count, which can be done either by increasing the excitation intensity or extending the recording time of the spectra (signal averaging) because the numerator (i.e. the Raman signal) of (1) increases in direct proportion to the Raman photon count and the denominator increases in proportion to the square root of the Raman, fluorescence, and background photon counts.

An interesting fact is that the intensity of fluorescence emission has been noticed to saturate with high enough pulsed laser excitation intensities, whereas the intensity of Raman scattering behaves linearly throughout the excitation intensity range, as depicted in Fig. 1(b) [20]. Basically, this laser-induced fluorescence saturation would mean that the denominator of (1) would increase slower, and thus the SNR faster, when the excitation intensity is increased compared to a situation with unsaturated fluorescence response. In other words, an additional improvement to SNR values could be achieved by exploiting the fluorescence saturation when samples that can stand high excitation intensities are measured (note that the N_F should be at least in the same order of magnitude as N_R, which is usually the case with fluorescent samples, to have a notable effect). The fluorescence saturation is explained by the finite number of excited states of molecules and by the finite lifetimes of these excited states [20], [21]. Even though this phenomenon was already found several decades ago, its effects on SNR in Raman spectroscopy has not yet been extensively studied and reported. It should be noted that in time-gated Raman spectroscopy we are dealing with non-stationary excitation (fluorescence lifetime of a sample is longer than the duration of the laser pulse), which means that a few orders higher excitation intensity is needed to achieve the fluorescence saturation compared to quasi-stationary excitation (the duration of the laser pulse is much longer than the fluorescence lifetime of a sample) [22].

The shot noise of detected events is not the only source to cause distortion to the spectra measured with time-resolved Raman spectrometers based on CMOS SPAD line sensors. Another important factor causing distortion to the spectra is the so-called timing skew of the sensors [15], [23]. The timing skew means that the start and end points of the time gate vary along the spectral range due to timing mismatches between the spectral points, i.e. between SPAD pixels in the sensor. This means that also both the time gate width and position (in the time domain) relative to the laser pulse vary along the spectral axis. Because of this timing skew, the photon count at different spectral points will vary even if the overall signal (including all the radiation from the sample and all the dark counts of the sensor) remain the same at the different spectral points. This photon count difference, i.e. sampling error, between subsequent spectral points is the reason for the additional distortion of the spectra.

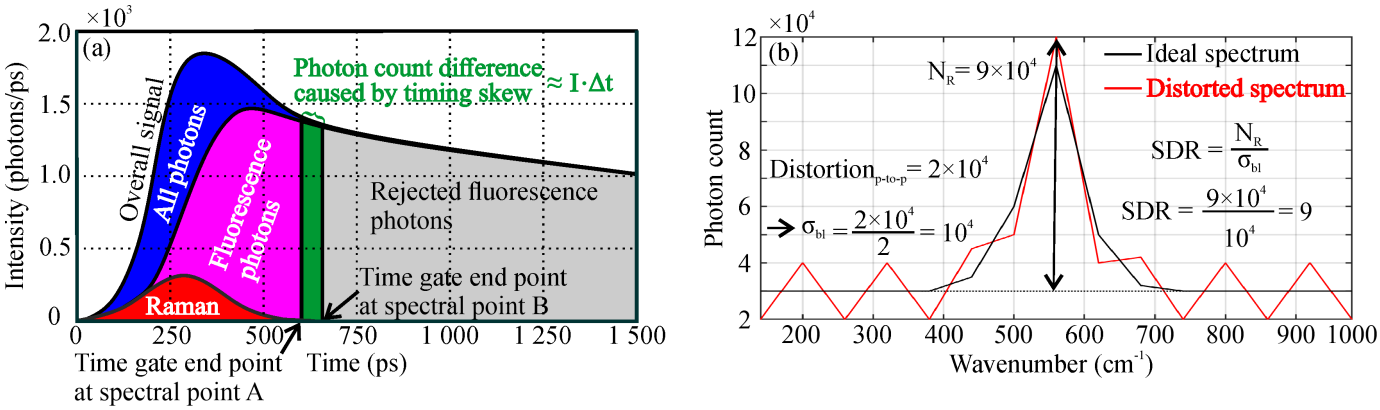

Fig. 2. (a) Principle of the photon count difference caused by the timing skew between spectral points in a line sensor and (b) the distortion that it causes to the spectra. In (b) is also shown an example how the SDR values were computed in this study. Here the signal intensities as a function of time are assumed to be identical at both spectral points A and B.

In this paper, we investigate the effects of fluorescence-to-Raman ratio, recording time (i.e. signal averaging) and excitation intensity on the quality of Raman spectra measured by using one of the furthest developed fluorescence-suppressed Raman spectrometers based on a time-resolved CMOS SPAD line sensor [15]. The objectives of this study are to provide information about the significance of the different causes behind the distortion of the measured Raman spectra in various measurement conditions to offer insights for future sensor circuit design and to provide general information about the possibilities to exploit the non-stationary high-intensity pulsed laser excitation to achieve additional improvement to the spectral quality owing to laser-induced fluorescence saturation.

II. Timing Skew and Signal-to-RMS-Distortion Ratio

The effect of the timing skew on the photon count difference at two example spectral points A and B is depicted in Fig. 2(a). The photon count difference between the spectral points A and B, which are assumed to have identical overall signal intensities for simplicity caused by timing skew can be computed by integrating the overall signal intensity from the time gate end point at the spectral point A to the time gate end point at the spectral point B resulting in the area of the green segment in Fig. 2(a). The area is much simpler to compute by approximating the green segment to be a rectangle and thus, the photon count difference can be computed with a simple equation:

$$\Delta N = I \cdot \Delta t \tag{2}$$

where I is the overall signal intensity (photons/ps) in the middle between the time gate end points A and B and Δt is the time difference between these time gate ending points, i.e. the timing skew.

If we now assume that a line sensor would only consist of the subsequent spectral points A and B shown in Fig. 2(a) (i.e. the pixels in the sensor would be ABABAB…), the timing skew would cause the sawtooth-like distortion shown in Fig. 2(b). Because the SNR described in (1) does not tell anything about the effects of timing skew on the quality of the measured Raman spectra, another quantity to define the spectral quality is also needed. Therefore, we also decided to define the overall quality and readability of the spectra by the term signal to root mean square (RMS) distortion ratio (SDR), which is mathematically expressed as follows:

$$SDR = \frac{N_R}{\sigma_{bl}} \tag{3}$$

where N_R is the detected Raman photon count and σ_{bl} is the baseline-corrected standard deviation of the distortion, i.e. the RMS distortion. For example, in the case of Fig. 2(b), the baseline-corrected standard deviation (σ_b in Fig. 2(b)) of the sawtooth-like distortion is the peak-to-peak amplitude of the distortion ($\text{distortion}_{p-to-p}$ in Fig. 2(b)) divided by 2, and the number of Raman photons is the amplitude of the Raman peak. By inserting the numbers to (3), we obtain the SDR value of 9 in Fig. 2(b). Section IV. A. describes how to derive the number of Raman photons and baseline-corrected standard deviation of the distortion in practice with real measurement data.

III. Measurement Setup and Test Principles

A. Fluorescence-Suppressed Raman Spectrometer Based on a Time-Resolved CMOS SPAD Line Sensor

A block diagram of the used CMOS SPAD-based Raman spectrometer is shown in Fig. 3(a). The spectrometer has a 16 × 256 time-resolved line sensor with an integrated 256-channel 3-bit on-chip time-to-digital converter (TDC). The system uses a 532 nm pulsed laser (Teem Photonics, Meylan, France, model: ANG-500P-CHS) as an illumination source. The pulse width (full width at half maximum), bandwidth and repetition rate of the laser are 160 ps, 0.11 nm and 350 kHz, respectively. The maximum pulse energy from the laser is 1 μJ but the desired output energy can be chosen by means of neutral density filters (ND filter in Fig. 3(a)).

A small portion of the laser pulse energy is guided to an optical detector by means of a beam splitter. The optical detector generates a logic level trigger signal that is passed through an off-chip digital delay unit to the 16 × 256 CMOS SPAD line sensor in order to bias the SPADs to the Geiger mode in which they can detect single photons. The off-chip

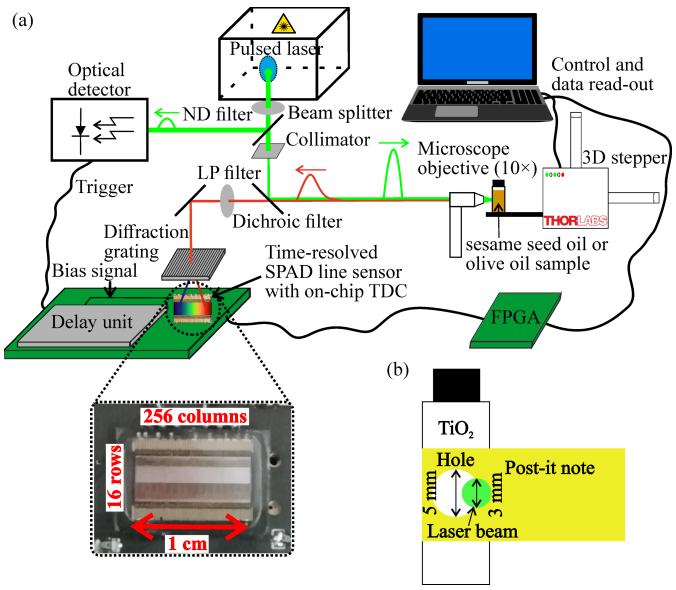

Fig. 3. (a) Block diagram of the Raman spectrometer based on a time-resolved 16 × 256 CMOS SPAD line sensor with an integrated 3-bit on-chip TDC. The block diagram also shows the measurement configuration for the evaluation of the effects of recording time and excitation intensity on spectral quality and (b) depicts the sample configuration for the evaluation of the effects of fluorescence-to-Raman ratio on spectral quality (measurements in (b) were done without the microscope objective to gain a wide enough laser beam, see text for details).

digital delay unit is used to compensate for the difference between the optical and electrical delays of the system so that the SPADs are biased, i.e. time-gated, to Geiger mode only during the photons arriving from the sample (red line in Fig. 3(a)) to collect all the Raman scattered photons and to reject most of the fluorescence emitted photons, as explained in the introduction.

The sensor has an integrated on-chip 256-channel 3-bit TDC (one channel per column) that measures the times of arrival of the backscattered photons. Each channel of the TDC have 8 time bins (numbered from 0 to 7) from which bins 1–6 are stabilized by a reference-locked delay line and thus, the resolution of these stabilized bins can be adjusted from ∼50 ps to ∼200 ps by modifying the reference clock frequency of the delay line. The longer unstabilized bin 0 is used to help adjust the timing of the stabilized bins 1-6, and bin 7 is an overrange bin that is used to detect the SPAD quenching signal generated by the CMOS logic to end an ongoing measurement cycle. The final time gate width is chosen in the data post-processing phase by selecting the analyzed time bins. In this study, the bin resolution was set to ∼100 ps and the photon counts of the bins 1–6 were summed up in post-processing, resulting in a time gate width of ∼600 ps.

Most of the laser pulse energy is guided through the collimator, dichroic filter (reflecting the laser pulse) and microscope objective (Olympus, Japan, model: Plan N, 10×/0.25 NA, spot size after objective ∼150 μm) to the sample. Rayleigh scattered photons from the sample are filtered by means of dichroic and longpass filters. A diffraction grating diverges the scattered photons so that the position of each SPAD column in the line sensors corresponds to a certain range of wavenumbers (the wavenumber resolution is ∼6 cm^{-1}).

TABLE I
MAIN CHARACTERISTICS OF THE USED RAMAN SPECTROMETER

	CHARACTERISTIC	VALUE
Laser		
	Wavelength	532 nm
	FWHM[a] pulse width	160 ps
	Repetition rate	350 kHz
	Maximum pulse energy	1 µJ
	Linewidth	0.11 nm
Sensor		
	Number of pixels	16 × 256
	Fill factor	26%
	Pitch	35 µm
	Wavenumber resolution	∼6 cm^{-1}
	Minimum bin width	52 ps
	Photon detection efficiency[b]	7–8%
	Maximum spectrum rate[c]	350 kHz
	Maximum timing skew along the spectral axis	±75 ps
	Average dark count rate[d]	128 Hz/µm^2
Spectrometer		
	FWHM[a] IRF[e]	225 ps

[a]Full width at half maximum [b]For the used technology (532–600 nm, 3V excess bias) [27], have not been measured with this sensor [c]Laser repetition rate is limiting [d]For the used pixels (hot pixel elimination) [e]Instrument response function

In addition, the system has a sample stage connected to a 3D stepper motor to be able to accurately move the sample and a field-programmable gate array control circuit (FPGA in Fig. 3(a)) connected to a computer to control the sensor circuit. All the data post-processing is done by using custom MATLAB scripts, including dark count removal (always) and filtering (only when mentioned, mean filtering with a window size of two subsequent points). The main characteristics of the spectrometer setup have been summarized in Table I, and a detailed description of the 16 × 256 CMOS SPAD sensor with an integrated 256-channel 3-bit on-chip TDC is given in [15]. The sensor can be said to be one of the furthest developed time-resolved CMOS SPAD line sensors for Raman spectroscopy at the moment [15, 24]. Other recent and advanced CMOS SPAD arrays for Raman spectroscopy and other biophotonics applications have been presented, for example, in [24]–[26].

B. Test Principles for Evaluating the Effects of Fluorescence-to-Raman Ratio on Spectral Quality

The purpose of these measurements was to investigate the quality of the measured Raman spectra as a function of fluorescence-to-Raman ratio. The measurements were conducted in the following steps: 1. Different color hole punched (ø = 5 mm) post-it notes were placed over a cuvette containing TiO_2 powder, as depicted in Fig 3(b), to achieve a large dynamic range of fluorescence-to-Raman ratios. 2. The microscope objective was removed to obtain a wide enough laser beam (still collimated beam, ø = 3 mm). 3. A 0.2 neutral density filter was placed in front of the laser to set the laser pulse energy to 0.63 μJ corresponding to average excitation intensity of 3.12 W/cm^2 with the laser spot size of 3 mm at the sample surface. 4. The collimated laser beam was adjusted to illuminate at the same time both the post-it note and the

TiO_2 powder through the hole in the post-it note, as shown in Fig. 3(b). 5. One million laser pulses were shot to the sample resulting in a recording time of 2.9 s with the laser repetition rate of 350 kHz (typically used acquisition time with this spectrometer also in more application-oriented studies).

The fluorescence-to-Raman ratio, which sometimes is also referred to as the fluorescence parameter ($\Phi = N_F/N_R$), was defined as the ratio between the amplitude of the Raman peak of TiO_2 at 635 cm^{-1} and the estimated fluorescence baseline under this Raman peak (polynomial fitting). These Raman and fluorescence photon count values were defined from the filtered and dark count corrected spectra and they were also used to compute the SNR values by employing (1) (here the fluorescence photon count also includes the background photons). The number of dark counts of the sensor for the computation of the SNR values was defined as the mean photon count of data that was measured in a dark room with normal Raman measurement configuration but without any sample (this data was also used in the dark count correction of the Raman spectra).

The fluorescence-to-Raman ratio was modified not only by using the different color post-it notes but also by adjusting the position of the laser beam in a way that it overlaps either more with the post-it note or more with the hole in the post-it note depending on which direction the fluorescence-to-Raman ratio was desired to be tuned. A total of 17 different fluorescence to Raman ratios were achieved with the used configurations, and the range of the ratios varied from 1.32 to 18.75 resulting in a dynamic range of 1:14. It should be noted that here the number of fluorescence photons means the number of residual fluorescence photons detected inside the 600 ps time gate and thus, the fluorescence-to-Raman ratios are much lower and SNR values are much higher than if the measurements were conducted by using a conventional CW Raman spectrometer.

C. Test Principles for Evaluating the Effects of Recording Time and Excitation Intensity on Spectral Quality

The purpose of these measurements was to investigate the quality of the measured Raman spectra as a function of recording time and excitation intensity. In addition, the aim was to observe fluorescence saturation and investigate its effects on the spectral quality. The measurements were conducted in the following steps: 1. The microscope objective was put back in its place to achieve higher excitation intensities. 2. The desired output pulse energy was set by placing the correct neutral density filter in front of the laser. 3. The sample was placed at the focus point of the laser (see also Fig. 3(a) in which the used measurement configuration is depicted). 4. Ten times one million laser pulses were shot to the sample with the laser repetition rate of 350 kHz to enable the selection of the recording time in the data post-processing from 2.9 s to 29 s with steps of 2.9 s (typically used acquisition times with this spectrometer also in more application-oriented studies).

The excitation energy range in these measurements was set from 0.016 μJ to 0.501 μJ corresponding to an average excitation intensity range from 31 W/cm^2 to 993 W/cm^2 with the laser spot diameter of 150 μm (the maximum energy (1 μJ) of the laser could not be used here because it is too high for the available optical fibers). The samples used here were sesame and olive oil, which have the unsaturated fluorescence-to-Raman ratios of 9.90 and 0.74, respectively, in the time-gated mode (derived as the ratio between the amplitude of Raman peak of lipids at 1657 cm^{-1} and the estimated fluorescence baseline under this peak). The corresponding CW mode fluorescence-to-Raman ratios were estimated to be 85 for sesame oil with the fluorescence lifetime of 2 ns and 7.7 for olive oil with the fluorescence lifetime of 2.5 ns [28].

IV. Results and Discussion

A. Effects of Fluorescence-to-Raman Ratio on Spectral Quality

Figure 4(a) shows the fitted theoretical SNR (dashed black line), measured SNR (solid blue line), SDR of filtered data (solid green line) and SDR of unfiltered data (solid red line) as a function of fluorescence-to-Raman ratio. Figures 4(b–e) show examples of filtered and dark count corrected Raman spectra with four different fluorescence-to-Raman ratios. It should be noted that a baseline correction of the spectra would make the spectra more readable, but this would affect neither the SNR nor SDR values because the baseline correction does not remove/filter noise or distortion (the baseline correction was not used here to show also the shape and intensity of the residual fluorescence emission inside the 600 ps time gate). The measured SNR values were computed from the filtered and dark count corrected spectra, as discussed in section III. B. The SDR values were computed with (3), which was shown in section II. The number of the Raman photons for the computation of the SDR values was defined from the same Raman peak as was defined the Raman photon count for the computation of the SNR values (TiO_2 peak at 635 cm^{-1}). The RMS distortion of both the filtered and unfiltered spectra was defined from baseline-corrected Raman spectra by computing the standard deviation of a wavenumber region from 688 cm^{-1} to 749 cm^{-1} (no Raman peaks). The fitted theoretical SNR values were computed by first fixing the Raman photon count to the mean value of the measured Raman photon counts at the different fluorescence-to-Raman ratios and then the theoretical fluorescence photon counts for the whole Raman-to-fluorescence dynamic range were derived based on this mean Raman photon count value. Mathematically this can be expressed as follows:

$$N_F(\Phi) = \overline{N_R} \cdot \Phi \tag{4}$$

where $\overline{N_R}$ is the mean Raman photon count with the different fluorescence-to-Raman ratios and Φ is the fluorescence-to-Raman ratio (i.e. fluorescence parameter). The dark counts of the sensor were set to zero when the fitted theoretical SNR values were computed.

Fig. 4(a) shows that the measured SNR curve fluctuates only moderately, and the shape of the curve is similar to the fitted theoretical SNR curve as could be anticipated. By comparing the SNR and unfiltered SDR curves it can be noticed that the unfiltered SDR curve always has lower values than the SNR curves. This is simply explained by the fact the SDR considers

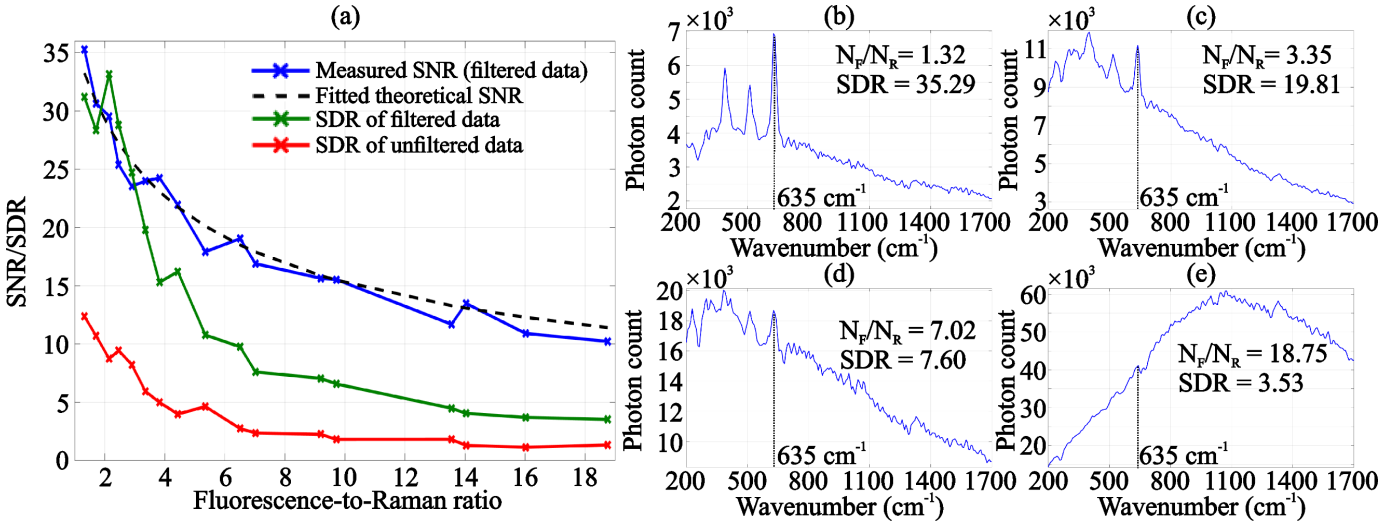

Fig. 4. (a) Measured SNR (solid blue line), fitted theoretical SNR (dashed black line), SDR of filtered data (solid green line) and SDR of unfiltered data (solid red line) as a function of fluorescence-to-Raman ratio. (b–e) Filtered and dark count corrected Raman spectra of TiO_2 with 1.32, 3.35, 7.02 and 18.75 fluorescence-to-Raman ratios, respectively. The vertical dotted lines point the Raman peak of TiO_2 at 635 cm^{-1}, which amplitude was used here to define the count of Raman photons.

both the shot noise and the distortion caused by the timing skew of the sensor meaning that the unfiltered SDR values can never beat the SNR values. Nevertheless, the SDR curve of the filtered data (mean filtering with window a size of two subsequent spectral points) gets higher values than the SNR curves with some of the lowest fluorescence-to-Raman ratios, but after the fluorescence-to-Raman ratio of 2.90 also the filtered SDR is conclusively beaten by the SNR curves. The reason why the filtered SDR values can beat the SNR values with the lowest fluorescence-to-Raman values is that the filtering does not have a notable effect on the number of detected photons, and thus on the SNR values, but rather the filtering reduces both the distortion caused by the shot noise and timing skew of the sensor, which decreases the RMS distortion and thus, increases the SDR values. As mentioned in section II, the distortion caused by the timing skew of the sensor increases in direct proportion to the overall signal level and therefore also the filtered SDR curve goes under the SNR curve with higher fluorescence-to-Raman ratios (i.e. with higher overall signal levels), as the filtering cannot anymore properly reduce the effects of increased distortion. The increase of the distortion caused by the timing skew as a function of overall signal intensity also explains why the SDR curves decrease steeper than the SNR curves.

The SDR values of filtered and unfiltered data were on average 35% and 79% lower than the measured SNR values. This shows the significance of the distortion caused by the timing skew of the sensor on the quality and readability of the recorded Raman spectra. The distortion results mostly from the variation of the time gate end point along with the spectral axis, as was shown in Figs. 2(a) and 2(b). The most important factors determining the magnitude of the distortion are the size of the timing skew, fluorescence-to-Raman ratio and fluorescence lifetime of the measured sample, as will be demonstrated with simulations in the next section. The timing skew of the sensor is covered in more detail in [15] and [23].

These results point out that the reduction of the timing skew play a key role when more challenging samples (i.e. samples with higher fluorescence-to-Raman ratios and with short fluorescence lifetimes, such as biological specimens) are desired to be measured with better SDR values, making the sensor circuit design extremely demanding. The timing skew of multichannel CMOS SPAD line sensors can never be completely avoided, regardless of how meticulously the sensor is designed, but their effects on the spectral quality can be computationally compensated for. A simple filtering was observed here to reduce the distortion to some extent, but it did not provide a comprehensive solution when the fluorescence intensity increased. Therefore, more sophisticated compensation methods are needed, one of which we demonstrated in [15]. The principle of the method in [15] is to measure a reference spectrum of a highly fluorescent sample having a smooth spectral shape to reveal the timing skew of the sensor along with the spectral axis and to use this information to compute correction factors for the timing skew at every spectral point. The drawback of the technique is that the spectral shape of the fluorescence between the reference sample and the measured sample should be similar for the method to work properly. The shape of the fluorescence of the different post-it notes had some variance, which can be seen from the spectra in Figs. 4(b)–(e), and thus the measurement of the reference spectra would have been challenging and time-consuming. This is why we decided not to use this compensation method here and thus, there is still demand for more practical and effective compensation methods.

Another challenge that is usually related to CMOS SPAD sensors are the already briefly mentioned dark counts of the sensors. The average dark count rate (DCR) of the sensor used here has been measured to be 128 Hz/μm^2 [15]. The DCR was defined only for the SPADs that are normally used in the measurements to achieve the best possible performance (hot pixel elimination, only 12 out of the 16 SPAD rows

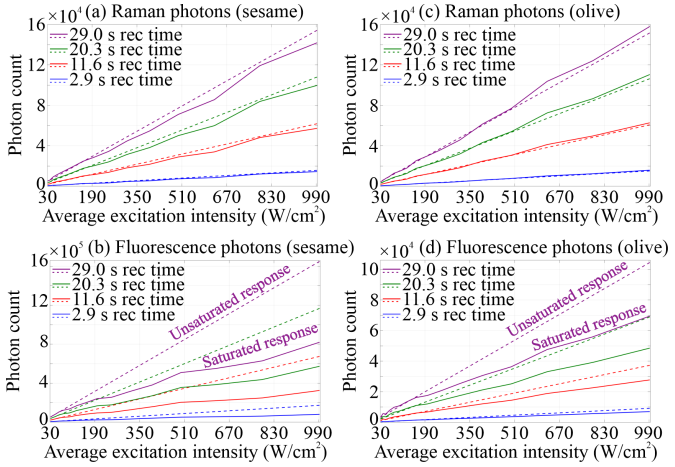

Fig. 5. Measured (solid lines) and fitted theoretical (dashed lines) Raman and fluorescence photon counts of (a)–(b) sesame oil and (c)–(d) olive oil as a function of average excitation intensity with four example recording times.

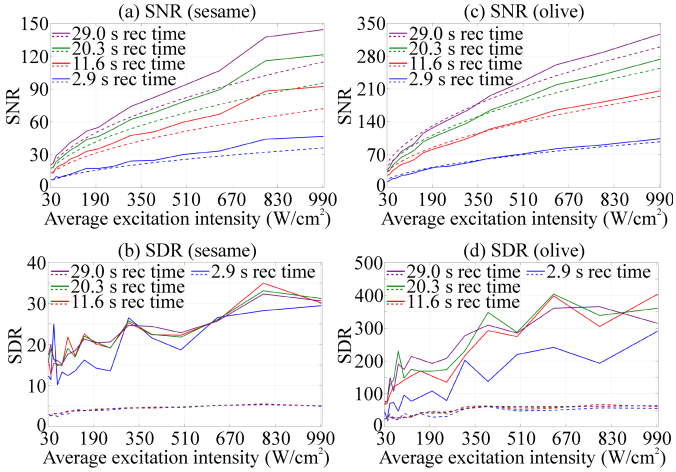

Fig. 6. Measured (solid lines) and theoretical unsaturated (dashed lines) signal-to-noise ratio (SNR) and filtered (solid lines) and unfiltered (dashed lines) signal-to-distortion ratio (SDR) of (a)–(b) sesame and (c)–(d) olive oil samples as a function of average excitation intensity with four example recording times.

are normally used). Nevertheless, the shot noise caused by the dark counts is not meaningful here, as can be seen by comparing the fitted theoretical SNR curve and the measured SNR curve in Fig. 4(a). The curves go almost hand in hand even though the dark counts were only considered when the measured SNR values were computed. The shot noise of the dark counts becomes problematic at lower overall signal levels. Besides, the distortion of the spectra caused by the variations in the dark count probability between the SPAD columns can be easily compensated for by subtracting the measured dark count distribution of the sensor from the measured spectral data as was also done in this study. Another not so significant issue causing some distortion to the spectra is the variation in the photon collection efficiency between the individual SPADs in the line sensor.

B. Effects of Recording Time and Excitation Intensity on Spectral Quality

Figures 5(a)–5(b) and 5(c)–5(d) show the measured (solid lines) and fitted theoretical (dashed lines) Raman and fluorescence photon counts of the sesame and olive oil samples, respectively, as a function of average excitation intensity with four example recording times. The Raman photon counts were defined from the amplitude of the Raman peak of lipids at 1657 cm^{-1}, and the fluorescence photon counts were defined from the estimated fluorescence baseline under this Raman peak (polynomial fitting). The fitted theoretical Raman photon counts as a function of excitation intensity for each of the recording times were computed by first scaling the measured Raman photon count of each excitation intensity with the scaling factor of I_n/I_{max} where I_n is the specific excitation intensity and I_{max} is the maximum excitation intensity (993 W/cm^2). Then, the mean values of these intensity-scaled Raman photon counts were used to derive the theoretical fitted Raman photon counts for each of the recording times (the dashed lines shown in Figs. 5(a) and 5(b)). The theoretical unsaturated fluorescence photon counts as a function of excitation intensity for each recording time were computed based on the measured fluorescence photon count with the lowest excitation intensity (31 W/cm^2). The main observation here is that the fluorescence emission indeed starts to saturate and behave nonlinearly when the excitation intensity is increased, whereas the intensity of Raman scattering does not saturate and behaves linearly. In addition, the fluorescence saturation was noticed to be greater with sesame oil than with olive oil.

Figures 6(a)–6(b) and 6(c)–6(d) show the measured (solid lines) and theoretical unsaturated (dashed lines) SNR and filtered (solid lines) and unfiltered (dashed lines) SDR values of the sesame and olive oil samples, respectively, as a function of average excitation intensity with four example recording times. The measured SNR and SDR values were computed in a similar way as in the previous section. The standard deviation for the RMS distortion was defined from wavenumber region of 1782–1847 cm^{-1} (baseline-corrected spectra). The theoretical SNR values with unsaturated fluorescence response were computed from the fitted theoretical Raman and fluorescence photon counts and again, the dark counts were set to zero when the theoretical values were computed. Figures 7(a)–7(b) and 7(c)–7(d) show example filtered and dark count corrected Raman spectra of the sesame and olive oil samples, respectively, with two different measurement settings.

As can be seen from Figs. 6(a) and 6(c), the measured SNR was observed to increase more strongly than the theoretical unsaturated SNR due to the fluorescence saturation. The difference between the measured and theoretical SNR values were greater with sesame oil because of its stronger fluorescence saturation. At best, the measured SNR values of sesame and olive oil were 26% and 9.1% higher, respectively, than the theoretical unsaturated SNR values. The effect of the fluorescence saturation on the SNR in the case of sesame oil is so strong that a 43% shorter recording time was enough to obtain the same SNR as with unsaturated fluorescence response as can be seen from Fig. 6(a) by comparing the solid red line and dashed green line (11.6 s vs. 20.3 s). On the other hand, Fig. 6(c) shows with low excitation intensities that the theoretical unsaturated SNR values of olive oil are slightly higher than the measured SNR values, which is explained by

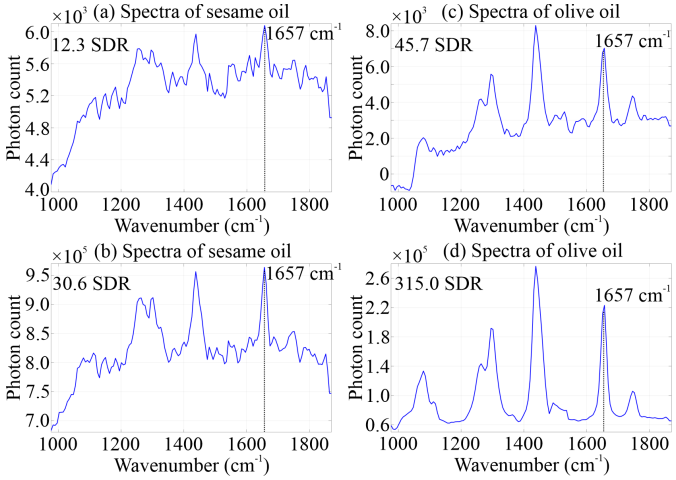

Fig. 7. Example filtered and dark count corrected Raman spectra of (a)–(b) sesame and (c)–(d) olive oil samples with two different measurement settings. In (a) and (c) the recording time and the average excitation intensity were 2.9 s and 31 W/cm^2, respectively, and in (b) and (d) they were 29 s and 993 W/cm^2, respectively. The vertical dotted lines point the Raman peak of lipids at 1657 cm^{-1}, which amplitude was used here to define the count of Raman photons.

the fact that the effect of the fluorescence saturation is weaker with lower excitation intensities and the saturation starts after a certain excitation intensity threshold (∼158 W/cm^2), as can be seen from Fig. 5(d). In addition, the dark counts of the SPADs were only considered in the computation of the measured SNR values and the effects of dark counts on the SNR are more evident when the overall signal level is low, as it is with olive oil when excitation intensity is kept low.

Measurements made with sesame oil had both lower SDR and SNR values than olive oil because of the shorter fluorescence lifetime and higher CW mode fluorescence-to-Raman ratio of sesame oil. These results also show that the unfiltered SDR values should never beat the SNR values (here the SDR values slightly beat the SNR values in some cases with low excitation intensities and short recording times due to inaccuracy in the determination of SNR and SDR values). A simple filtering was again noticed to reduce both the distortion caused by the shot noise and timing skew with lower fluorescence-to-Raman ratios (olive oil), but the filtering was found out to be insufficient to compensate for the distortion with higher fluorescence-to-Raman ratios (sesame oil), as can be seen by comparing the filtered SDR and SNR curves in Figs. 6(a)–(d). The filtered SDR values of olive oil were generally higher than the SNR values, whereas the filtered SDR values of sesame oil were lower than the SNR values.

Another interesting observation from Figs. 6(a)–(d) is that the extension of the recording time (signal averaging) did not markedly improve the SDR values of sesame oil and with olive oil, the SDR values did not further improve when the recording time was extended over 11.6 s. Moreover, the increase of the excitation intensity did not improve the SDR values as strongly as it does improve the SNR values (theoretical unsaturated SNR values increase in direct proportion to the square root of the excitation intensity and the measured SNR values increase even stronger due to fluorescence saturation). Once again, the explanation for these observations is the timing skew of the sensor. As has been mentioned several times, the distortion of the spectra caused by timing skew is directly proportional to the overall signal level. The increases of the excitation intensity and extension of the recording time increase both the Raman and overall signal intensities in the same proportion under unsaturated conditions and thus, they do not improve SDR because both the Raman signal and distortion increase in the same proportion. Despite all of this, the SDR values were noticed to increase as a function of excitation intensity, and the actual reason for this is the observed fluorescence saturation. The explanation why the SDR values of olive increase when the recording time is extended from 2.9 s up to 11.6 s is that the overall signal level with the shortest recording times is so much lower that the distortion caused by timing skew is not yet dominating. Therefore, improvement to the SDR values can be achieved by extending the recording time, i.e. by signal averaging, due to the improved SNR.

The effect of the timing skew on the spectral quality was also evaluated by simulations from which an example result is shown in Fig. 8. The simulation model first generates the relative time-domain photon distributions of the modelled sample based on the entered CW-mode fluorescence-to-Raman ratio and fluorescence lifetime (see a virtual example in Fig. 2(a) in section II). After this, the simulation model computes the variation in the number of detected photons caused by the timing skew between adjacent spectral points with multiple timing skew sizes (see (2) and Fig. 2(a) in section II). The variance in the number of detected photons between adjacent spectral points causes the sawtooth-like distortion in the formed spectrum and the SDR values can be derived as discussed in section II and illustrated in Fig 2(b). The initial time gate end point in the simulations was defined as the point in time where the overall signal intensity decreased to ∼85% of its maximum value because this kind of time gating works properly with most of the samples making the simulation model independent of the absolute value of the laser pulse width. From the simulation results in Fig. 8 it can be observed, for example, that with a sample having the CW mode fluorescence-to-Raman ratio of 85 and the fluorescence lifetime of 2 ns, which are similar to sesame oil, the unsaturated and unfiltered SDR value of ∼2.7 cannot be exceeded if the timing skew between adjacent spectral points is 20 ps or more even if the sensor is otherwise assumed to be ideal. This corresponds well with the experimental results observed in this study with sesame oil, as can be seen from the unfiltered SDR values in Fig. 6(b) with the lowest excitation intensities (fluorescence saturation with the higher excitation intensities enhance the SDR values over the simulated unsaturated maximum value). Therefore, the timing skew of the sensor between adjacent spectral points can be estimated to be around 20 ps based on the obtained results, which is in line with the findings presented in [23].

In addition, the importance to reduce the effects of the timing skew can be further understood by the following example from the measurements: The unfiltered SDR value achieved with the longest recording time (29 s) and the highest excitation intensity (993 W/cm^2) of sesame oil was 5.08, as can be seen from Fig 6(b). By following the solid violet and

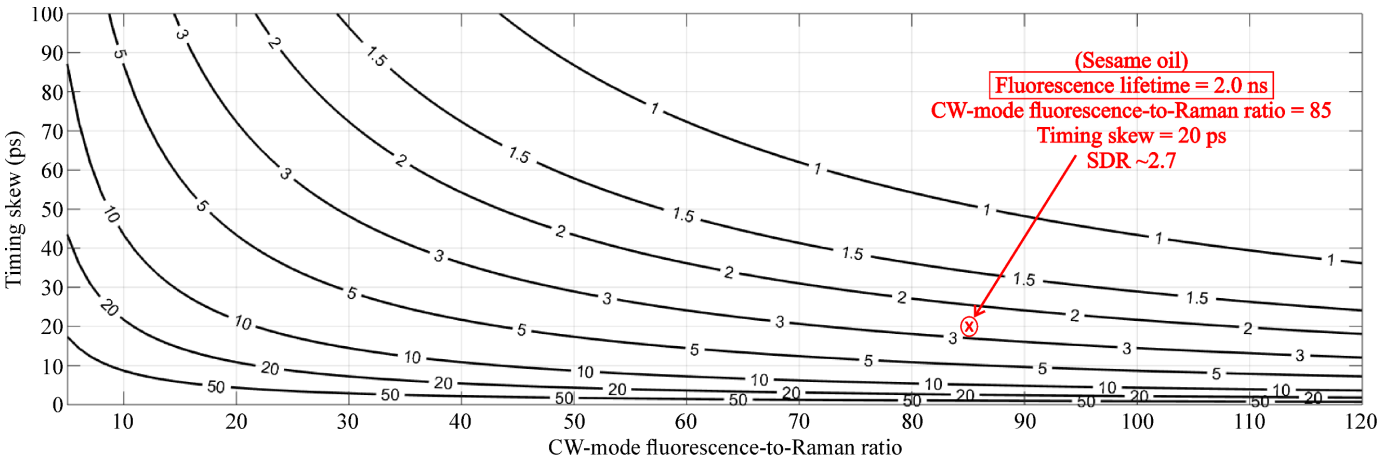

Fig. 8. Simulated maximum unfiltered SDR values as a function of timing skew between adjacent spectral points and CW-mode fluorescence-to-Raman ratio. The fluorescence lifetime of the sample in the presented simulation was set to 2 ns.

blue lines in Fig. 6(a) (measured SNR curves with recording times of 29 s and 2.9 s) it can be evaluated that with a sensor without the timing skew, 27 times higher SDR value could be reached with the same measurement settings (29 s recording time and 993 W/cm^2 excitation intensity) or alternatively, twice as high SDR values could be reached with a 90% shorter recording time (2.9 s) and with 95% lower excitation intensity (49.8 W/cm^2).

The findings presented here further emphasize the importance to make the effort to avoid timing skew when SPAD line sensors are designed and the importance to develop more effective methods to computationally compensate for the timing skew of an implemented sensor. With more precise timing properties of a sensor, the extension of the recording time (signal averaging) and the increase of the excitation intensity could be exploited more efficiently especially with challenging samples to gain better quality Raman spectra. Alternatively, the better timing properties of a sensor would mean that the recording time needed for a certain SDR value with a certain sample could be decreased markedly, which is important in many practical applications with strict duration limits, such as process control and clinical Raman measurements.

V. Conclusions

This paper investigated the spectral quality of a fluorescence-suppressed Raman spectrometer based on a time-resolved 16×256 CMOS SPAD line sensor with an integrated 256-channel 3-bit on-chip TDC when fluorescent samples were measured. The results showed that the SDR (signal-to-RMS-distortion ratio) values of the recorded filtered and unfiltered Raman spectra were on average 35% and 79% lower than the SNR values defined from the shot noise of all detected events with 1:14 dynamic range of fluorescence-to-Raman ratios. Basically, this means that the noise of the spectra with SPAD lines sensors consists not only of the shot noise but also of the distortion caused by the timing skew of the sensors. It was shown in the measurements that the timing skew becomes the dominating noise source with high overall signal (including both Raman and fluorescence signals) levels. It should be remembered that the timing skew is a universal issue with SPAD line sensors because it can never be completely avoided due to component mismatches in the sensor circuits. The distortion caused by the timing skew increases with highly fluorescent samples in the same proportion as the Raman signal when the recording time is extended and/or excitation intensity is increased due to the higher overall signal level. Therefore, because of the timing skew neither the extension of the recording time (signal averaging) nor the increase of the excitation intensity can be fully exploited to gain better quality Raman spectra, emphasizing the importance to reduce the timing skew in designing future sensors and the need for more effective computational compensation methods for the timing skew. With lower overall signal levels other noise sources, such as the dark counts of sensors, come into the picture and obviously, must also be considered when sensors with large dynamic range are being designed.

An increase in the SDR values as a function of excitation intensity was obtained in the measurements even though the Raman signal and the distortion caused by the timing skew increase in the same proportion when the excitation intensity is increased. The reason for this was found to be the non-stationary laser-induced fluorescence saturation. The fluorescence photon counts behaved nonlinearly, whereas the behavior of Raman photon counts was linear as a function of excitation intensity explaining the observed improvement of the SDR values. At best, 26% improvement to the SNR value was observed owing to fluorescence saturation, or alternatively, a certain SNR value was maintained with 43% shorter recording time in the presence of fluorescence saturation. The results showed that an additional improvement to the spectral quality of highly fluorescent samples can be achieved by using high-intensity non-stationary pulsed laser excitation due to the fluorescence saturation if the measured sample can stand the high excitation intensity over its fluorescence saturation threshold without damage.

Although that this study showed that there is still a lot of work to do to harness the full potential of time-resolved CMOS SPAD line sensors for Raman spectroscopy, it should be noted that the CMOS SPAD-based Raman spectroscopy has already shown its potential in various conventionally challenging applications, such as Raman analyses through

single optical fibers, analysis of fluorescent pharmaceuticals, quantification of pickle liquor and chemical imaging of human teeth and rare earth element bearing rocks [16], [29]–[32]. The field of CMOS SPAD-based Raman spectroscopy is still relatively young (the first conference paper about the topic was published less than a decade ago [11]) but the developments made in the sensor architectures and performances promise a bright future for the time-resolved CMOS SPAD-based Raman spectroscopy.

REFERENCES

[1] D. Yang and Y. Ying, "Applications of Raman spectroscopy in agricultural products and food analysis: A review," *Appl. Spectrosc. Rev.*, vol. 46, no. 7, pp. 539–560, Oct. 2011.

[2] E. L. Izake, "Forensic and homeland security applications of modern portable Raman spectroscopy," *Forensic Sci. Int.*, vol. 202, nos. 1–3, pp. 1–8, Oct. 2010.

[3] K. Kong, C. Kendall, N. Stone, and I. Notingher, "Raman spectroscopy for medical diagnostics—From *in-vitro* biofluid assays to *in-vivo* cancer detection," *Adv. Drug Del. Rev.*, vol. 89, pp. 121–134, Jul. 2015.

[4] C. Krafft and V. Sergo, "Biomedical applications of Raman and infrared spectroscopy to diagnose tissues," *Spectroscopy*, vol. 20, nos. 5–6, pp. 195–218, 2006.

[5] T. Vankeirsbilck *et al.*, "Applications of Raman spectroscopy in pharmaceutical analysis," *Trends Anal. Chem.*, vol. 21, no. 12, pp. 869–877, Dec. 2002.

[6] E. B. Hanlon *et al.*, "Prospects for *in vivo* Raman spectroscopy," *Phys. Med. Biol.*, vol. 45, no. 2, pp. R1–R59, Feb. 2000.

[7] M. L'Heureux, "Analysis of the state of the art: Raman spectroscopy," *Spectroscopy*, vol. 30, no. 6, Jun. 2015.

[8] J. R. Lakowizc, *Principles of Fluorescence Spectroscopy*, 3rd ed. New York, NY, USA: Springer, 2006, ch. 1, pp. 1–26.

[9] D. V. Martyshkin, R. C. Ahuja, A. Kudriavtsev, and S. B. Mirov, "Effective suppression of fluorescence light in Raman measurements using ultrafast time gated charge coupled device camera," *Rev. Sci. Instrum.*, vol. 75, no. 3, pp. 630–635, Mar. 2004.

[10] P. Matousek *et al.*, "Fluorescence suppression in resonance Raman spectroscopy using a high-performance picosecond Kerr gate," *J. Raman Spectrosc.*, vol. 32, no. 12, pp. 983–988, Dec. 2001.

[11] I. Nissinen *et al.*, "A sub-ns time-gated CMOS single photon avalanche diode detector for Raman spectroscopy," in *Proc. Eur. Solid-State Device Res. Conf. (ESSDERC)*, Helsinki, Finland, Sep. 2011, pp. 375–378.

[12] J. Kostamovaara, J. Tenhunen, M. Kögler, I. Nissinen, J. Nissinen, and P. Keränen, "Fluorescence suppression in Raman spectroscopy using a time-gated CMOS SPAD," *Opt. Express*, vol. 21, no. 25, p. 31632, Dec. 2013.

[13] L. Pancheri and D. Stoppa, "A SPAD-based pixel linear array for high-speed time-gated fluorescence lifetime imaging," in *Proc. ESSCIRC*, Athens, Greece, Sep. 2009, pp. 428–431.

[14] I. Nissinen, A. Länsman, J. Nissinen, J. Holma, and J. Kostamovaara, "2×(4×)128 time-gated CMOS single photon avalanche diode line detector with 100 ps resolution for Raman spectroscopy," in *Proc. ESSCIRC*, Bucharest, Romania, Sep. 2013, pp. 291–294.

[15] I. Nissinen, J. Nissinen, P. Keranen, D. Stoppa, and J. Kostamovaara, "A 16 × 256 SPAD line detector with a 50-ps, 3-bit, 256-channel time-to-digital converter for Raman spectroscopy," *IEEE Sensors J.*, vol. 18, no. 9, pp. 3789–3798, May 2018.

[16] K. Ehrlich *et al.*, "PH sensing through a single optical fibre using SERS and CMOS SPAD line arrays," *Opt. Express*, vol. 25, no. 25, pp. 30976–30986, Dec. 2017.

[17] Y. Maruyama, J. Blacksberg, and E. Charbon, "A 1024×8, 700-ps time-gated SPAD line sensor for planetary surface exploration with laser Raman spectroscopy and LIBS," *IEEE J. Solid-State Circuits*, vol. 49, no. 1, pp. 179–189, Jan. 2014.

[18] J. Kekkonen, J. Nissinen, J. Kostamovaara, and I. Nissinen, "Distance-resolving Raman radar based on a time-correlated CMOS single-photon avalanche diode line sensor," *Sensors*, vol. 18, no. 10, p. 3200, Sep. 2018.

[19] J. Kekkonen, J. Nissinen, and I. Nissinen, "Depth analysis of semi-transparent media by a time-correlated CMOS SPAD line sensor-based depth-resolving Raman spectrometer," *IEEE Sensors J.*, vol. 19, no. 16, pp. 6711–6720, Aug. 2019.

[20] A. Chekalyuk, V. Fadeev, G. Georgiev, and Z. Nickolov, "Application of laser induced saturation of molecular fluorescence for lifetime measurements," *Opt. Commun.*, vol. 38, no. 3, pp. 177–181, Aug. 1981.

[21] V. I. Yuzhakov, K. G. Yevsyukhina, and S. V. Patsayeva, "Laser-induced saturation of fluorescence for complex organic molecules," in *Proc. ALT Int. Conf. Laser Surf. Process.*, Limoges, France, May 1998.

[22] S. V. Patsayeva, V. I. Yuzhakov, and V. Varlamov, "Laser-induced fluorescence saturation for binary mixtures of organic luminophores," in *Proc. Laser Spectrosc. Opt. Diagnostics, Novel Trends Appl. Laser Chem., Biophysics, Biomed. (ICONO)*, Moscow, Russia, Feb. 1999.

[23] J. Holma, I. Nissinen, J. Nissinen, and J. Kostamovaara, "Characterization of the timing homogeneity in a CMOS SPAD array designed for time-gated Raman spectroscopy," *IEEE Trans. Instrum. Meas.*, vol. 66, no. 7, pp. 1837–1844, Mar. 2017.

[24] C. Bruschini, H. Homulle, I. M. Antolovic, S. Burri, and E. Charbon, "Single-photon avalanche diode imagers in biophotonics: Review and outlook," *Light Sci., Appl.*, vol. 8, no. 1, p. 87, Sep. 2019.

[25] A. T. Erdogan *et al.*, "A CMOS SPAD line sensor with per-pixel histogramming TDC for time-resolved multispectral imaging," *IEEE J. Solid-State Circuits*, vol. 54, no. 6, pp. 1705–1719, Jun. 2019.

[26] A. Usai, N. Finlayson, C. D. Gregory, C. Campbell, and R. K. Henderson, "Separating fluorescence from Raman spectra using a CMOS SPAD TCSPC line sensor for biomedical applications," *Proc. SPIE*, vol. 10873, Mar. 2019, Art. no. 108730R.

[27] D. Mosconi, D. Stoppa, L. Pancheri, L. Gonzo, and A. Simoni, "CMOS single-photon avalanche diode array for time-resolved fluorescence detection," in *Proc. 32nd Eur. Solid-State Circuits Conf.*, Montreux, Switzerland, Sep. 2006, pp. 564–567.

[28] I. Nissinen, J. Nissinen, P. Keränen, and J. Kostamovaara, "On the effects of the time gate position and width on the signal-to-noise ratio for detection of Raman spectrum in a time-gated CMOS single-photon avalanche diode based sensor," *Sens. Actuators B, Chem.*, vol. 241, pp. 1145–1152, Mar. 2017.

[29] T. Lipiäinen *et al.*, "Time-gated Raman spectroscopy for quantitative determination of solid-state forms of fluorescent pharmaceuticals," *Anal. Chem.*, vol. 90, no. 7, pp. 4832–4839, Apr. 2018.

[30] B. Heilala, A. Mäkinen, I. Nissinen, J. Nissinen, A. Mäkynen, and P. Perämäki, "Evaluation of time-gated Raman spectroscopy for the determination of nitric, sulfuric and hydrofluoric acid concentrations in pickle liquor," *Microchem. J.*, vol. 137, pp. 342–347, Mar. 2018.

[31] J. Kekkonen, M. A. J. Finnilä, J. Heikkilä, V. Anttonen, and I. Nissinen, "Chemical imaging of human teeth by a time-resolved Raman spectrometer based on a CMOS single-photon avalanche diode line sensor," *Analyst*, vol. 144, no. 20, pp. 6089–6097, Sep. 2019.

[32] S. Romppanen *et al.*, "Time-gated Raman and laser-induced breakdown spectroscopy in mapping of eudialyte and catapleiite," *J. Raman Spectrosc.*, early access, May 2019, doi: 10.1002/jrs.5622.

Jere Kekkonen received the M.Sc. degree in medical and wellness technology from the University of Oulu, Finland, in 2018, where he is currently pursuing the Ph.D. degree in electrical engineering with the Circuits and Systems Research Unit. His research interest includes novel functionalities and applications of time-resolved Raman spectroscopy systems based on CMOS SPAD line sensors.

Tuomo Talala received the M.Sc. (Math) and M.Sc. (Tech.) degrees from the University of Oulu, Finland, in 2010 and 2018, respectively, where he is currently pursuing the Ph.D. degree in electrical engineering with the Circuits and Systems Research Unit. His research interests include the development of integrated sensors and data post-processing techniques for time-resolved Raman spectroscopy.

Jan Nissinen received the M.Sc. (Eng.) and Dr.Tech. degrees in electrical engineering from the University of Oulu, Finland, in 2002 and 2011, respectively. He has been a Postdoctoral Researcher with the Circuits and Systems Research Unit, University of Oulu, since 2011. His research interests include the design of analog and mixed-signal integrated circuits for pulsed time-of-flight laser rangefinders and for pulsed Raman spectroscopy.

Ilkka Nissinen (Member, IEEE) received the M.Sc. (Eng.) and Dr.Tech. degrees in electrical engineering from the University of Oulu, Finland, in 2002 and 2011, respectively. Since 2018, he has been an Associate Professor of Analogue and Mixed-Signal Microelectronic Circuit Design with the Circuits and Systems Research Unit, University of Oulu. His research interest includes the design of time interval measurement architectures for the integrated sensors of pulsed time-of-flight laser technologies.